Bond type and discretization of non-muscle myosin II are critical for simulated contractile dynamics

D.B Cortes, M. Gordon, F. Nédélec, A.S. Maddox

Running Head: Tuning motor bonding and coarse-graining

ABSTRACT

Contractile cytoskeletal networks drive cell shape changes in many contexts including cytokinesis, the physical division of one cell into two. The primary source of force generation in contractile networks is non-muscle myosin II (NMMII), a molecular motor that assembles into bipolar ensembles that bind, slide, and crosslink actin filaments (F-actin). The multivalence of NMMII ensembles and their many roles have confounded the resolution of crucial questions including how the motors in NMMII ensembles impact each other's binding, how the number of NMMII subunits affects network dynamics, and what affects the relative contribution of ensembles' crosslinking versus motoring activities. Since measurements of ensembles are difficult, modeling of actomyosin networks has aided in discovering the complex behaviors of NMMII ensembles. Myosin ensembles have been modeled via several strategies with variable discretization/coarse-graining and unbinding dynamics, and while most result in global contractile behaviors, it remains unclear which strategies most accurately depict cellular activity. Here, we used an agent-based platform, Cytosim, to model NMMII ensembles via several strategies. Comparing the effects of bond type, we found that for discretized ensembles, only catch-slip motors exhibited processive translocation on immobilized F-actin. Conversely, all unbinding dynamics estimations allowed coarse-grained ensembles to translocate, though catch motors were the slowest and least processive. On simulated contractile rings, all motor types drove constriction, though again, only catch-slip NMMII motors generated effective contractile forces when fully discretized. In addition, rings fragmentation or coiled in all cases except those of fully discretized catch-slip motors. Changes in network connectivity not only affect contractile speed, as previously reported, but also seem to affect the amount of ring fragmentation and coiling. Together our results support the importance of

modeling strategy chosen for NMMII ensembles, in terms of both discretization of motor units and bond type, for accurately estimating connectivity and providing more efficient contractility.

STATEMENT OF SIGNIFICANCE

Agent-based simulations of contractile networks have provided many insights into the mechanics of actomyosin contractility, such as that which drives cytokinesis, the final step of cell division. Past attempts to predict the mechanics and dynamics of non-muscle contractility have lacked a consensus on how to best model the non-muscle myosin II motor ensembles. These highly complex ensembles of approximately 32 motors are responsible for driving contractility. Here, we comprehensively explore different methods for modeling non-muscle myosin II ensembles individually and within the context of contractile rings. We show that different levels of ensemble coarse-graining and different motor bonding behaviors under load can both have profound effects on contractile network dynamics.

INTRODUCTION

Cytokinesis, the last stage of cell division, is the physical division of one cell into two. Cytokinesis is powered by a specialized band of cortical cytoskeleton known as the contractile or cytokinetic ring, which forms in anaphase and constricts to invaginate the plasma membrane and partition the cytoplasm. The essential components of the cytokinetic ring include non-muscle myosin II (NMMII) motor ensembles, filamentous actin

(F-actin), and crosslinkers including anillin, alpha-actinin, and septins (1). Conventional and super-resolution live imaging have provided important insights into actin dynamics and alignment during cytokinetic ring formation (2, 3), and the relative quantities of ring components throughout constriction (4, 5).

Although the main components that form the cytokinetic ring are known, the molecular mechanisms that drive closure dynamics remain unclear. Specifically, the roles of NMMII are poorly understood.

NMMII is capable of sliding actin filaments through its motoring activity (6–10). However, NMMII motor ensembles are also robust F-actin crosslinkers (6, 7, 11, 12). Thus, it is unclear whether NMMII ensembles generate contractile forces through motor activity-dependent polarity sorting of actin filaments, which would induce filament buckling in a crosslinked network (13–16), or through passive crosslinking of depolymerizing or treadmilling F-actin (17, 18). The former hypothesis predicts complete failure of cytokinesis with motor-dead NMMII, while the latter predicts that motor activity is dispensable. Work with mammalian cultured cells and the budding yeast, *S. cerevisiae,* provided evidence for contractility in the presence of motor-domain lacking NMMII (17) or motor-deficient NMMII (19), suggesting that NMMII primarily contributes as a crosslinker. However, similar experiments with *Drosophila* and *C. elegans* suggested NMMII motor activity is required for cytokinesis in embryonic cells and tissues (20, 21). Separation of motor and crosslinking activities *in vivo* is confounded by observations that some motor-dead isoforms bind F-actin more tightly or for longer than wild-type NMMII and are thus crosslinking gain-of-function (20). Interestingly, contractile speed is not a linear function of the abundances of both NMMII and non-motor crosslinkers, as intermediate levels were

observed to confer optimal contractile dynamics (3, 15, 22, 23). Defining the relative contributions of NMMII motoring and crosslinking to contractility will not only shed light on the mechanics of cytokinesis, but also the myriad of other contexts in which NMMII drives non-muscle contractility, such as cell motility and epithelial morphogenesis.

Extensive biochemical and biophysical work has shown that NMMII forms large bipolar ensembles with 12-30 motor domain pairs extending from the ends of a rod formed by the bundled coiled-coil tails of the NMMII heavy chains (8, 12, 24). The complex architecture of NMMII ensembles further confounds attempts at understanding their explicit roles in cytokinesis.

While biophysics, biochemistry and cell biology have revealed much about the contributions of NMMII to non-muscle contractility, a complementary approach is agent-based modeling, wherein collective behaviors emerge from the explicit simulation of the components and their interactions. Published agent-based models of actomyosin networks have incorporated actin filament treadmilling (17, 18, 22), filament buckling (15, 16), varied crosslinker/motor ratios (15, 16, 22), and complex motor ensemble strategies (25–29). However, the relevance of these models to force generation in actomyosin rings is limited by how actin and myosin were modeled. Specifically, many employ dimeric processive motors representing myosin VI, a motor that runs in the opposite direction than NMMII (3, 15, 16, 29). Work on NMMII motor ensembles depicted its interaction with only a single actin filament (25, 26). Motor ensembles have been depicted either as multiple discrete binding entities (each representing one or a few motor heads) or as a single binding entity (coarse-grained; representing all the motors on one end of the filament). In the latter case, it is difficult to calculate aggregate binding and unbinding

rates that correctly depict the behavior of multiple motors (22). The former is computationally intensive and may not realistically depict the complex crosstalk among motor subunits in an ensemble. Thus, when deciding how to best model the NMMII ensembles in an actomyosin system, one is faced with a tradeoff between simplicity and realism, for which there is no established solution.

Non-covalent bonds are generally described as slip bonds, where bond lifetime decays exponentially with increasing applied external force (Fig. 1A, top). Some molecular motors fall into this regime (30); *in silico* unbinding dynamics akin to slip bonds emerged when simulations consider the ATP-hydrolysis cycling rates of muscle myosin II measured in vitro in calculating unbinding events (31). By contrast, statistical models of collections of muscle myosin II motors acting together exhibit emergent catch-bond dynamics (25, 26). Catch bond dynamics can be described generally by an exponential increase in bond lifetime as force is applied up to a critical point where the bond lifetime may plateau before eventually rupturing under extreme force-load (Fig. 1A, bottom). Atomic force microscopy performed with purified rat muscle myosin II heavy meromyosin (HMM) (32) and optical tweezer experiments with single muscle myosin II ensembles (33, 34) have suggested that some myosins can be described by catch bond dynamics. Catch-slip bonds exhibit a biphasic response to applied force; initially force-load increases the bond lifetime up to a critical point (the catch regime), after which the bond lifetime decreases (the slip regime) (Fig. 1A, middle). It is unknown, however, how such differences in bond behavior under load affect crosslinking and motoring activities of motor ensembles, and ultimately impact actomyosin network architecture and contractility.

We sought to identify a suitable representation of NMMII that would provide realistic motoring and crosslinking functions, as desired to simulate the mechanisms of cytokinesis and other events of non-muscle contractility. Using the agent-based modeling software, Cytosim (35) (www.cytosim.org), we compared several approaches to modeling NMMII motors in the context of a cytoskeletal ring, consisting of actin-like filaments (referred to as “filaments” for simplicity), NMMII-like motor ensembles, and non-motor crosslinkers approximating the contributions of anillin (filament-motor scaffolding), septin (x-y crosslinking) and α-actinin (filament crosslinking). Whereas previously we simulated NMMII filaments as simplified motor clusters represented by single actin binders on either side of stiff rods (Fig. 2A) (22), here we compared this simplified model with simulations of motor ensembles with increasingly discretized motoring subunits. Herein we also compared the behaviors of motor ensembles with heads exhibiting slip, catch, and catch-slip bond dynamics. We demonstrated that all three of these approximations can generate contractile networks, though they differ dramatically in their outcome, particularly the global contraction rate. We offer recommendations on motor modeling for optimization of calculation time, connectivity realism, and biological predictability.

METHODS

Cytosim base code

Cytosim, an open-source Brownian motion simulation program (35), was used to perform all agent-based simulations in this work. Within Cytosim, filaments are modeled as segmented lines, with bending elasticity as determined by the persistence length of F-

actin, this is ~15 µm, resulting in a bending modulus of 0.06 pN·µm^2. Filament movements are determined by an over-dampened Langevin equation ($\xi\ \mathrm{dx/dt} = (x\ ,\ t) + B(t)$), that accounts for system viscosity, drag (as determined by the Stokes' radius of the filament), thermal energy (KbT), the bending elasticity of the filament and the forces exerted by connectors (35). Actin dynamics were based on previous models (17, 18), and include depolymerization primarily at pointed ends and polymerization primarily at barbed ends, with a net treadmilling rate of 0.1 µm/s and net depolymerization rate of 0.002 µm/s (36). Generic crosslinkers were modeled as described (15), to represent a crosslinker like α-actinin, bearing a single actin-binding domain at each end of a small rigid rod. We also included scaffolds that represent anillin and septins, which were modeled as short rods with binding hands linked by stiff springs. Unbinding dynamics of crosslinkers and scaffolds were modeled according to Kramer's theory: $k_{off} = k_0 \exp(F_t/F_0)$; where k_0 is the unloaded unbinding rate, F_0 is the characteristic unbinding force, and F_t is the force felt by crosslinkers bridging filaments at time t.

NMMII motor head unbinding dynamics were calculated by one of several methods which yield either slip bond, catch bond, or catch-slip bond dynamics. Motoring speed was calculated at each simulation frame by the formula: $V_t = V_0\ (1 - F_t\ /\ F^0_{stall})$ (except for in the case of parallel cluster model motors (PCM); where V_0 is the unloaded motor speed, F_0 is the stall force, and F_t is the load force at timepoint t. NMMII complexes were simulated as bipolar couples with actin-binding motoring domains attached at either end of a filament. Each actin-binding motor domain was modeled to simulate the dynamics of one or several NMMII motoring heads (between 1-16) for total NMMII valence of 32 motors.

The base code of Cytosim was modified to enable two new functionalities as follows:

1) Catch bond approximation: $k_{\text{off}}(F) = \sum_{j=1}^{Nt} \frac{1}{r(j)} \prod_{k=1}^{j-1} \frac{g(k)}{r(k)}$ for Nt motors with unbinding dynamics, where $\mathrm{r(j)}$ is the reverse rate of motor unbinding given j post-power stroke motors, $\mathrm{g(k)}$ is the forward rate of binding given k post-power stroke motors and $\mathrm{r(k)}$ is the reverse rate of unbinding given k post-power stroke motors. Bound-motor mean velocity approximation: $\mathrm{V_t} = \sum_{i=1}^{Nt} v_i \hat{p}_i(\infty)$ where v_i is the complex velocity given i bound motors and $\hat{p}_i(\infty)$ is the probability of an average i bound motors over infinite time (26).

2) Catch-slip bond approximation: $k_{\text{off}}(F) = k^0_{\text{off}} [\alpha_{\text{catch}} \exp(-F\, x_{catch} / k_B T) + \beta_{\text{slip}} \exp(F\, x_{slip} / k_B T)$ for motor unbinding dynamics (25, 32).

Gliding motor simulations

These simulations were set up to measure the movement of motor ensemble without interference from load and connectivity. All simulations were initiated with an environmental viscosity of 1 Pa.s, similar to the viscosity of *C. elegans* zygote cytoplasm (37) and a thermal energy of 4.2 pN·nm. For this setup, NMMII motor ensembles were monopolar complexes that could bind to only one filament per binder at a time. Motors, either discrete or coarse-grained, were arrayed on one end of a stiff rod representing half a NMMII ensemble. Filaments 11 microns in length were placed horizontally, all pointing with the plus (barbed) ends on the right. These filaments were irreversibly immobilized. Motor ensembles were initially placed on the left side and allowed to walk for 200 or 400

seconds, depending on simulation conditions. Their movements were evaluated from positions recorded every second. For greater detail, see sample code in the supplement (Table S4).

Motor ensemble speeds were calculated as follows: Positional information about all motor ensemble backbones (the “myosin fiber”) was pooled with information about the binding-state of all binders attached to each ensemble fiber backbone. Translocation speed was calculated for an ensemble only when the preceding time frame and the current time frame showed at least one of its n binders bound to an immobilized filament. Translocation was then calculated as the change in position (in nanometers) over time (each frame is 1 second apart). Average translocation was calculated per ensemble over the duration of either the ensemble walking off the other end of an immobilized filament or 400 seconds, whichever happened first. A population average and standard deviation was calculated for 120 ensembles of each type.

For visualization, kymographs were rendered in FIJI (ImageJ). The simulation state was rendered every second, and the PNG images imported in FIJI. A line ~12 microns in length was drawn over one of the immobilized filaments in each simulation and the Kymograph plugin was used to construct a kymograph for 100 timepoints from each simulation. Bound motor ensembles were visualized as colored dots, resulting in kymographs of streaks or lines moving from left to right (position) down the y-axis (time) of the generated images.

Motor complex binding percentage was calculated for all motors on all like-ensembles at each time point of the simulation, as well as for all ensembles as a unit (an ensemble was considered bound so long as 1 of its binders was actively bound to an immobilized

filament). Averages and standard deviations were then calculated for each population of ensembles.

Contractile ring simulations

Ring simulations were set up as follows. All ring simulations were initiated with environmental parameters akin to those of our actin walking simulations in a circular space with a radius of 1.5 microns. At initiation, the space was populated with 360 actin filaments of 1 ± 0.3 microns long, 800 anillin, 600 septin and 600 actinin molecules. Actin filaments were placed in a 120 nm thick ring 10 nm from the edge of the circular space, tangent to the circle. The crosslinkers were placed just overlapping and outside of the actin filaments. The simulation was allowed to generate binding events without moving the filaments for two seconds of simulated time, and then 360 myosin ensembles were added to the ring space. Following another 2 seconds of simulated time during which only binding and unbinding could occur, the Brownian dynamics were enabled, and run for 400 seconds of simulated time. All crosslinkers except for alpha-actinin were simulated as filaments adorned with binding components. For simplicity, the abundance of components was constant throughout the simulations. However, unbound components could diffuse far enough away from the ring to never reincorporate, and thus be non-productive. For more details see the sample code (Table S1).

Motor ensembles were simulated differently based on the coarse-graining procedure. However, all ensembles were simulated as 300 nm-long rigid rods, representing bundled NMMII tails, with a variable number of binding components with motoring activity adjusted

to represent different valences of NMMII motors. In the case of the most discretized ensembles, 16 binders were attached to either end of the rigid rods, regularly spaced apart in the first 20 nm of either end. In this case, each binder represented a single motor which could independently bind to and motor along single filaments. More coarse-grained binders represented up to all 16 motors on either end of the myosin rod were still limited to binding only one filament.

Circle-fitting of Contractile Ring Simulations

Ring closure dynamics were quantified by estimating the speed of radial change. Given the highly fluid nature of the ring in our simulations an average radius R first needed to be calculated for all time points. To robustly approximate radius over time we automated the fitting of a circle to the ring. From Cytosim, we first exported coordinate points for the centers of all filaments representing anillin at each time point of our simulations as .CSV files. These CSV files were reorganized for readability then ported as tabular data into MATLAB (MathWorks) as structures consisting of coordinate matrices for each frame of simulated data.

The Pratt method (Pratt 1987) was then used to fit a circle to each set of coordinate points representing the ring, allowing us to estimate R(t), from which we derived raw radial speed (R(t+u)-R(t))/u in nm/s where u is an increment of time. We also used the radius measurements to calculate ring closure percentages as 100 $[\,1 - R(t) / R(0)\,]$. The ring perimeter was also calculated for each frame.

Simulated rings generally closed off-center, asymmetrically and frequently with many coils and bends. As such, we reduced fitting-error noise by performing a moving average of speed, closure and perimeter data with a window of five frames. We also controlled for the possibility of a ring closing partway and then opening up after falling apart. This was done by first detecting whether any frame reported a radius over 112% the size of the previous frame as well as whether any trend in size increase could be detected over 4 frames. If at any point in time one of these conditions was met, all following time frames were discarded for population averaging.

Once all data were smoothened for each individual simulation, we combined the datasets for all like simulations and calculated average and standard deviation of speed, percent closure and perimeter. Average speed data were smoothened via a five-frame window moving average, as before (22).

Actin Connectivity Estimations

We extended Cytosim report functions to export meaningful connectivity data specifically for this project. First, to report out motor ensemble-based connectivity, we coded in a function that found all motor ‘couples’ connected to a myosin backbone and reported the unique identifier of all filaments (one fiber per couple) interacting with those couples. These data, in CSV format, were then ported to MATLAB where a simple function detected the number of unique filaments interacting with each motor ensemble at each time point. The interaction number was then averaged for all motor ensembles throughout the simulation or up until 80% closure was achieved. The average number of unique

ensemble-filament interactions was then used to estimate a total number of filament-filament interactions: [$\lambda = \delta \times (\delta - 1) / 2$], where λ is the connectivity and δ is the number of filaments interacting with an ensemble. The λs for all motor ensembles in the simulation were then used to calculate an average λ which was applied to calculate the total connectivity provided by NMMII ensembles.

A similar approach was followed to quantify total connectivity, resulting from anillin- and septin-like connections. The connectivity of α-actinin-like couples was estimated by first measuring the average number of all actinin entities successfully bound to two filaments, as this is the only configuration possible that creates connections, for which $\lambda = 1$. The different connectivity numbers were summed to calculate the grand total in these simulations.

RESULTS

Coarse-grained motor ensembles with slip bond dynamics generate contractility

NMMII is found in cells assembled into bipolar ensembles with numerous (~32) motors on each end (8, 12, 38, 39). This multiplicity poses a challenge for agent-based modeling, wherein the behavior of each component is explicitly simulated. We and others have modeled NMMII ensembles, in a simplified fashion, as rods with one or a few actin-binders on either end (22, 27, 40), but both the degree of motor ensemble discretization and the bond type have varied among published models. Here, we use Cytosim, an over-

dampened Langevin physics simulator (35), to systematically test the effects of both these variables on motor ensemble behavior and network dynamics.

We first represented the motor ensembles as two actin binders connected by a stiff rod, as previously (22). The effective parameters of these binders were calculated by assuming that the asynchronous hydrolytic cycles of the motor domains have an additive effect on binding rate, unbinding force, and stall force. Hence the binding rate increased, while the unbinding rate conversely decreased, according to the number of motors represented by an actin binder. As in published Cytosim-based models, the lifetime of motors on the filaments was dictated by slip-bond dynamics.

We began by simulating monopolar NMMII ensembles composed of a single actin binder attached to one end of a linear backbone of 300 nm in length (Fig. 2A). This configuration allowed us to specifically characterize motor behavior, since monopolar motor ensembles could not crosslink but could walk along immobilized parallel filaments. Under these conditions, motor ensembles moved processively at 147.2±2.7 nm/s (Fig. 2A; Movie 1), which is comparable to the unloaded speed parameter of 150 nm/s (6, 7, 12) specified in our simulations.

To next test how our ensembles behave in an actomyosin meshwork, we simulated motor ensembles on ring-shaped networks. To recapitulate the bipolar architecture of NMMII ensembles, we placed actin binders, each representing 16 motors, on either side of a 300 nm-long rod (28-32 total motors) (8, 12, 24). Simulated rings had a starting radius of 1.5 microns, approximating that of the fission yeast *S. pombe* at onset of cytokinesis (Fig. 2B). Starting amounts of all ring components were set according to protein counting measurements performed in *S. pombe* (Table S1 in the supporting material) (4, 5). To

quantify ring closure, we automated fitting of a circle to the band of ring components at every simulated timepoint (Fig. S1; Methods). Simulated ring contraction reached a radial speed of 98.2±6.1 nm/s (Fig. 2E).

In vivo, cytokinetic ring contraction generally occurs with a relatively constant speed, but with gradual acceleration until approximately half closure (41). To test whether our simulated rings behaved realistically in this way, we examined ring kinetics. Rings simulated with NMMII ensembles as described above reached maximum speed when the ring was 35% closed. Thus, while maximum speed was preceded by a period of acceleration as expected, the maximum was reached earlier than *in vivo.*

Closure completed in about 40 simulated seconds (n=20) (Fig. 2B, E; Movie 2). However, after reaching approximately 13% of the initial size, or 87% closure, our automated method could no longer reliably fit circles to the data. Therefore, hereafter, closure above 80% was considered to be completed. Rings remained globally connected throughout cytokinesis, with all filaments connected by motor ensembles and non-motor crosslinkers. Together, these simulations indicate that depicting NMMII ensembles as rods with two actin binders dictated by slip-bond dynamics can recapitulate some but not all general features of cytokinetic ring closure.

Discretized motor ensembles with slip bond dynamics are not contractile

Connectivity, or the level at which the filaments are crosslinked in a network, is increasingly appreciated as a key factor regulating contractility (3, 15, 16, 22) by modulating force generation and force transmission. While our previous modeling

strategy for multimerizing motor ensemble behavior was mathematically simple and functional, it could not realistically account for the connectivity afforded by the multiple motor heads of NMMII motor ensembles, due to the underrepresentation of filament-binding sites per ensemble. Therefore, we next explored the effects of modeling NMMII motor complexes with more filament binders as this may increase connectivity.

To this end, each motor in an ensemble was represented as an independent filament binder. Motor subunit binding and unbinding dynamics were as reported for single motors (22, 25). First, 16 motor heads were arrayed on one end of a rigid rod (Fig. 2C). On immobilized filaments, these monopolar complexes translocated at 107±15.8 nm/s, slower and were bound less frequently (41.6±7.21%) than the coarse-grained (80.3±3.1%) version of the same ensembles (Fig. 2C).

We then simulated rings populated with these motor ensembles, now in bipolar conformation, with complexes of 16 motors on either end of the 300 nm-long rigid rod. Such simulated rings exhibited global contractility (Fig. 2D, F; Movie 3), but only reached maximum speeds of 2.4±2.1 nm/s and did not close past 16% in 400 seconds of simulated time (Fig. 2F). Thus, discretizing slip bond heads made rings approximately 40-fold slower than rings populated with coarse-grained motor complexes. In addition to their low speed, these rings failed to complete closure due to fragmentation (20/20) (Fig. 2D). Despite fragmenting, these rings were generally percolated, containing a single cluster of interconnected actin filaments (19/20). Therefore, motor ensembles depicted as rods with discretized, slip-bonding motor subunits motored with a significantly slower speed and failed to confer the connectivity of physiological rings.

As mentioned above, discretized monopolar complexes were frequently unbound during the simulation runtime, never fully reaching the opposite ends of the immobilized filaments (Fig. 2C). We reasoned that the basis for this reduction of processivity related to the percentage of time each motor head was bound (akin to the duty ratio). Indeed, discretized filament binders had a 4±2.2% duty ratio, while coarse-grained actin binders had a duty ratio calculated at 80.5±3.1%. We tested whether increasing the duty ratio by decreasing the unbinding rate of single motors in the discretized ensemble to that calculated for the coarse-grained complex was sufficient to confer increased translocation to discretized motor ensembles. A 10-fold reduction in unbinding rate resulted in a duty ratio of 49±14% which was paralleled by an increase in translocation speed to 148.3±1.6 nm/s (Fig. S2B). When simulated in rings, these motors with artificially low unbinding rate had a 50% duty ratio and resulted in global contractile speeds of 2.2±0.7 nm/s with maximum closure of 27% (Fig. S3A, C, D; Movie 4). Interestingly, while slow in contractility, these rings coiled abnormally as they constricted (Fig. S2A). Importantly, there is no biophysical basis to justify altering the unloaded binding and binding dynamics of NMMII-like motors in this manner. There is evidence, however, that NMMII complexes exhibit reduced unbinding rates under force-load (25, 26, 32).

Coarse-grained ensembles with catch bond dynamics generate contractility

Motor complexes can be coarse-grained by rigorously calculating the collective stochastic behaviors of all motor subunits. A statistical mechanics approach was used to approximate the collective binding, unbinding and motoring dynamics of muscle myosin II complexes (Parallel Clusters) for a range of numbers of motors approximated by a

single actin binding entity (Parallel Cluster Model; PCM) (25, 26, 40). Using biophysical parameters measured for muscle myosin II, these models recapitulated the highly processive behavior of myosin complexes (12, 25). Importantly, the PCM model exhibits catch bond dynamics. We posited that modeling NMMII using this PCM approach could increase ensemble processivity and thus efficient ring constriction. Thus, we adapted this PCM method into Cytosim (see Methods). We first simulated muscle myosin II complexes with published motor parameters, as a single actin binder, representing 16 motors, on one end of a rigid rod (26). When placed on immobilized filaments, these motor ensembles translocated at speeds of 298.8±3.2 nm/s and were bound 87.8±2.73% of the time (Fig. 3A). This speed, faster than the motor head speed parameter of 150 nm/s, results from the PCM model which calculates a bound velocity for PCs based on force-load and number of motors bound (26) (Table S1).Thus, our execution of the PCM in Cytosim yielded qualitatively different results than our slip bond ensemble simulations and published *in vitro* results (8, 12, 24).

We then seeded rings with bipolar ensembles bearing these muscle motor entities exhibiting catch bonding. Rings contracted rapidly, with a radial speed of 131±11.2 nm/s, and fully constricted past 80% closure within 20 seconds of simulated time (Fig. 3B, E; Movie 5). As with slip bond NMMII ensembles, these rings folded and coiled, but unlike most rings with slip bond motors, did not fragment (Fig. 3B). These results demonstrate that the PCM method can generate global contraction with muscle myosin II parameters.

We next implemented the PCM model to simulate coarse-grained motor ensembles with the binding and unbinding rates of NMMII instead of those of muscle myosin II. Such NMMII motor ensembles on fixed filaments moved at 12.0±0.1 nm/s and

remained bound 99.5±1.2% of the time (Fig. 3C). When rings were populated with these motors, rings contracted with maximum speeds of 6.5±1.2 nm/s and closed to ~80% (Fig. 3D, F; Movie 6). Thus, modeling NMMII ensembles as fully coarse-grained collectives with catch-bonding dynamics results in slow contractility. These slower dynamics, along with the pronounced coiling as with slip-bond ensembles, suggested that fully coarse-grained catch-bonding NMMII motors cannot accurately represent the global dynamics of cytokinetic rings *in vivo.*

Intermediate coarse-graining of catch bond ensembles affects contractility

Motor ensembles modeled with the PCM approach were shown to exhibit different binding dynamics and effective motor velocity depending on the number of motor subunits represented by single entity (the collective parallel cluster; PC) (26). Therefore, we next used our agent-based modeling approach to test the effect on motoring activity of simulating ensembles as entities representing 16, 8, 4, 2, and 1 motor(s) each. For all of these simulations, the total number of motors simulated on either side of ensembles remained at 16. As such, the number of actin binding sites changed from 16 (where each PC represented a single motor), to 8, 4, 2, and 1 (where the sole PC represented all 16 motors).

Immobilized filaments were seeded with monopolar ensembles representing each of the combinations described above to compare their mobility independently of their crosslinking ability. As reported above, fully coarse-grained (single entity) NMMII ensembles translocated processively, but moved at slow speeds around 14.5 nm/s (Fig.

4A-C). Increasing the discretization (decreasing the number of motors represented by each PC) of NMMII ensembles resulted in decreased translocation speeds down to just over 4 nm/s for fully discretized ensembles (Fig. 4A; Fig. S3; Table S2). The calculated duty ratios for all of these ensembles were high, ranging from 98% for fully discretized ensembles to above 99% for fully coarse-grained ensembles (Fig. 4D).

Actin rings simulated with all PCM variations of NMMII ensembles exhibited similar constriction rates of ~4-6 nm/s and final closure to ~50-60% for all PCM simulations except those which were fully coarse-grained, which had closure rates of 6.5 nm/s and closed further to ~70% (Fig. 4B,C). Therefore, independent of multimerization, catch-bonding NMMII motors remain associated with the same filament for long times, moving much slower than previous ensemble modeling approaches and slower than the expected translocation rates (8, 12, 24).

Discretized and coarse-grained catch-slip bond ensembles generate contractility

Although the PCM method rendered motors more processive and allows ring constriction, both discretization and coarse-graining strategies presented problems. Discretized PCM NMMII ensembles translocated at a fraction of the expected speed (8, 12, 24) (Fig. 4A). Second, coarse-graining PCM ensembles slightly increases contractility but significantly increases coiling and fragmentation of simulated rings with increased coarse-graining, suggesting worsening network structure (Fig. S3).

Furthermore, individual muscle myosin II motors have been described as exhibiting not pure catch or slip unbinding dynamics, but rather catch-slip unbinding dynamics with

actin filaments (Fig. 1A) (32). A mathematical method for approximating catch-slip bond dynamics was initially described for single muscle myosin II motor heads (32), and later applied to model ensembles of both muscle and non-muscle myosin II motors via addition of a term representing the number of motors per ensemble (25).

Here we first implemented the initial method in Cytosim to simulate NMMII ensembles with fully discretized motors interacting with filaments via catch-slip binding dynamics (32). We simulated motors with properties of individual NMMII motors (3.85 pN stall force, 0.35/s binding rate, 1.71/s unloaded unbinding rate, and 150 nm/s unloaded speed), but unbinding rate under force-load calculated by the catch-slip bond equation (see methods). Monopolar ensembles of 16 NMMII motors seeded on immobile filaments translocated with speeds of 126.1±6.6 nm/s, and with 23.3±8.1% of all actin binders and 64.8±4.48% of all motor ensembles bound at any given moment. The ensembles, possessing 16 motor domains each, remained associated with the filament for the entirety of their run-length (Fig. 5A; Movie 1). In sum, motor ensembles with discretized heads exhibiting catch-slip bond behavior recapitulate the behavior of NMMII ensembles *in vitro* (6, 7, 12). When bipolar ensembles with 16 of these discretized motors on each end were simulated on rings, closure reached maximum contractile speeds of 75.4±2.9 nm/s. These rings closed past 80% (20/20) and did not fragment or coil (19/20) (Fig. 5B, E; Movie 7).

A simple additive coarse-graining of these ensembles to represent all 16 motors per side as a single actin binder was achieved by multiplying the binding and unbinding parameters of a single motor by 16. Monopolar ensembles with single coarse-grained catch-slip motor complexes translocated at speeds of 131.7±7.3 nm/s on immobilized

filaments (Fig. 5C). Interestingly, while fully discretized and coarse-grained catch-slip motors translocated with essentially the same speed, rings seeded with bipolar coarse-grained catch-slip ensembles contracted more slowly than rings with discretized catch-slip motors, with maximum speeds of 48±6.7 nm/s. These rings closed completely past 80% (20/20) but exhibited significantly more coiling than the rings with discretized motors (Fig. 5D, F; Movie 8) and comparable to the coiling observed for coarse-grained slip motor ensembles (Fig. 2B).

Together these results suggest that catch-slip ensembles, when fully discretized, provide adequate contractility and result in a more realistic network shape than other modeling approaches. Coarse-graining catch-slip ensembles appears to negatively affect actin network shape and decreases the effectiveness of force generation and transmission, which could be due to reduced ring connectivity.

Discretized NMMII ensembles provide greater connectivity to the network

Connectivity can modulate actomyosin network contractility (3, 15, 16, 22), and our results clearly show a change in actin network architecture driven by changes in motor ensemble discretization (Fig. 4; Fig. 5). Thus, we sought to quantify the NMMII ensemble-based connectivity of actin filaments in our ring simulations.

The agent-based nature of Cytosim allowed us to extract the number of filaments linked together by all motor-entities on each ensemble in ring simulations. This number was used to calculate a connectivity number for each simulation type (see Methods). Briefly, from the list of motor couples which comprise an individual NMMII ensemble, we

count the number of distinct filaments to which the motors are attached. This number, δ, is then used to calculate network connectivity provided by this ensemble, $\lambda = [\delta \times (\delta - 1) / 2]$, which is the number of unique filament pairs being connected.

All fully discretized ensembles provided significantly more connectivity to the actin network than the same type of motor in a fully coarse-grained ensemble (Table S3). In the case of fully discretized slip bond motor ensembles, we saw ~4.3 connections between filaments per motor ensemble, which is significantly less than for catch bond ensembles, with ~240, and catch-slip bond motor ensembles, with ~190. All three bond-types resulted in significantly less connections between filaments when fully coarse-grained (~2 for catch bonds, ~0.9 for slip bonds and ~0.85 for catch-slip bonds).

Regardless of the bond type (slip, catch, or catch-slip), fully discretized ensembles provided substantially (~5- to ~50-fold) more connectivity to the actin network than the same type of motor in a fully coarse-grained ensemble (Table S3). Bond type also influenced the connectivity conferred by motor ensembles. Fully discretized slip bond motor ensembles provided a connectivity of ~4; catch bond ensembles a connectivity of ~240 and catch-slip bond motor ensembles a connectivity of ~190.

We also calculated the connectivity conferred by other simulation components septin, anillin, and alpha-actinin to estimate total connectivity for each simulation setup. For catch-slip simulations, fully discretized ensembles increased total connectivity to ~80,000, or roughly 4 times greater than the total connectivity for simulations with coarse-grained ensembles (~24,000). Similar results were obtained for catch bond ensembles when comparing discrete versus coarse-grained ensembles (connectivity of ~76,000 vs ~22,000, respectively; Table S3). It is worth noting that for intermediate coarse-grained

catch bond ensembles, the total connectivity was basically unchanged by increasing the coarse-graining to include more than 4 motor units per PC. Despite motor-based connectivity continuing to decrease with further aggregation (Fig. 6A), septin and anillin-like components appeared to compensate for this decrease. Due to the previous description of the relationship between filament connectivity and constriction, we sought to validate a similar relationship in our data. Indeed, fitting of the relationships between either total connectivity and maximum speed or motor-based connectivity and maximum closure speed suggested a quadratic dependence where intermediate connectivity yielded the fastest maximum closure speeds (Fig. 6A, B).

Modulating connectivity by non-motor crosslinkers affects contractile speed

Modulating connectivity changes the contractile speed of generalized *in silico* contractile networks; specifically, intermediate connectivity allows maximal contractile speed and force generation (3, 15, 16, 22). Since the level of PCM motor ensembles coarse-graining affects connectivity, we expected to observe a similar relationship in our simulated rings. Our initial simulations however did not offer sufficient variability to test this hypothesis. Thus, we simulated rings with varying number of septin-like fibers, which changed the total connectivity linearly (Fig. 6C). This resulted in a broad range (10,000-220,000) of network connectivity, while all other aspects of the simulations remained constant. PCs of 8 motors were chosen to ensure total connectivity could be modulated an order of magnitude lower and higher than the default condition. In this extended set, the maximum speeds depended quadratically on the total connectivity, with maximal speeds achieved around a connectivity score of ~150,000 (roughly triple that predicted

by varying connectivity through motor ensemble coarse-graining) (Fig. 6D). Thus, our findings support the growing consensus that optimal contractility is achieved with intermediate connectivity, but also suggest that the effects of changing connectivity via motor or non-motor crosslinkers are measurably different.

DISCUSSION

Summary

Here, we compared three strategies for modeling NMMII ensembles during cytokinetic ring contraction. We showed how motor performance and collective behavior are affected by the model used to approximate unbinding dynamics under load, and by the level of coarse-graining of NMMII ensembles. Further we demonstrated that the choice of a NMMII model affects total network connectivity and structure. Overall, while several approaches can produce contractile networks, they have distinct complex effects on dynamic network architecture, which are important to consider as the field moves closer to biologically-contextualized predictive models.

The effects of NMMII ensemble coarse-graining

Type II myosin motors form large bipolar ensembles ranging from tens of motors for non-muscle variants (6–8, 12) to hundreds for muscle variants (25, 26). There exists a range of approaches for simulating myosin II ensembles, from fully coarse-grained agents to complexes made up of many fully discretized motoring units (16, 25–27, 29,

32). Here, we compared both strategies as well as intermediate levels of coarse-graining in the case of catch bond motors.

In general, increasing discretization of motor subunits within ensembles increased network connectivity. By contrast, as ensembles are more coarse-grained, collective binding of the constituent motor domains was represented by increased binding rate, but each ensemble interacted with fewer filaments. The reduction of connectivity by coarse-graining, in turn, destabilized the network architecture of rings, which exhibited large coils and shed filaments from the main ring network.

Interestingly, fully discretized ensembles exhibited very poor mobility and resulted in the slowest contractile speeds for slip bond and catch bond simulations. For catch bond ensembles specifically, slow translocation likely results since fully discretized ensembles had 97% of all actin binders bound at any given moment, and therefore had excess connectivity that limited force propagation (15, 16). On the opposite extreme, fully coarse-grained ensembles drive faster ring contraction but rings are less stably organized due to lower connectivity. In sum, our work suggests that, while less molecularly accurate, fully coarse-grained catch or slip bond motor ensembles provide useful approximations for global contractile network dynamics.

Connectivity conferred by NMMII ensembles

The major influence of motor ensemble discretization on filamentous network architecture and stability strongly imply a causal connection with connectivity.

Taking catch bond ensembles as an example, we saw that motor ensemble-based connectivity continued to decrease as coarse-graining was increased. Total connectivity, however, plateaued around 20,000 after ensembles were coarse-grained to PCs of 4 motors each. Considering all but the fully coarse-grained case, a best-fit quadratic of either total connectivity versus speed or motor ensemble-based connectivity versus speed predicts that intermediate connectivity (around 50,000 for total connectivity) would provide the fastest contractility (Fig. S3A, B). This is in accordance with recent work suggesting that intermediate connectivity provides maximal contractility where stability is achieved but remodeling is possible (15, 16, 22). Applying this best-fit curve to catch-slip motor data we see a potential explanation for the slower contractility of rings with fully coarse-grained ensembles (with connectivity of ~24,000) versus discretized ensembles (with connectivity of ~80,000).

Slip bond motor ensembles, unlike catch-slip and catch motor ensembles did not follow the trend of increased connectivity with increased discretization. Instead, while motor-based connectivity decreased when coarse-grained, total connectivity was roughly unaltered by discretization. Because slip bond ensembles are such poor binders, especially when discretized, they contribute a minimal amount (~1-7%; Table S3) to overall ring connectivity *in silico*. Thus, it is not surprising that overall connectivity is so similar for the two simulation types. Despite a minimal effect on connectivity, however, coarse-graining slip-bonding ensembles renders them significantly better at generating contractility. This is likely due to the decreased unbinding rate (which might be underestimated by our simplistic model) of coarse-grained slip-bonding ensembles, which increases their processivity (Fig. 2).

These results support the growing consensus that network connectivity profoundly impacts contractility. Our systematic comparisons reveal how the level of coarse-graining and the nature of simulated bond can both affect network connectivity, and thus impact the emergent properties of actin network structure and contractility. Importantly, slip bond motor ensembles, regardless of discretization, do not affect connectivity, suggesting these may be less useful for generating biologically predictive simulations.

In cells, NMMII and non-motor crosslinkers both contribute to actomyosin network connectivity. Interestingly, in our simulations maximal contractile speed is reached at different levels of total connectivity depending on whether it is modulated by motor ensemble properties or by total number of non-motor crosslinkers (Fig. S3D). This highlights a crucial difference between motors and non-motor crosslinkers: how these agents behave under force load. As currently modeled, catch and catch-slip bond motor ensembles make significantly stronger and longer-lived connections between filaments under load than any of the non-motor crosslinkers, all of which are modeled with slip bond behavior. Therefore, lower total connectivity is required to reveal contractile braking effects when the increase in connectivity is achieved through modulation of motor ensembles. Future work beyond our results with fully discretized ensembles will distinguish whether motor ensembles confer as much to connectivity *in vivo*, or if there is a need for more accuracy in motor properties *in silico*.

Outlook

We focused on varying strategies used to model motor ensembles. A methodical comparison of diverse modeling strategies will also inform depiction of other components but the lack of biophysical measurements affects these efforts. For example, F-actin dynamics affect contractility in many simulations (17, 18), but since the *in vivo* rates of F-actin treadmilling, turn over, and depolymerization are not known. Modeling the connectivity provided by crosslinkers will require measurements including bundle geometry and unbinding force. In addition, a bounding membrane that both provides connectivity and resists deformation is missing from most models (29). Finally, because cytokinesis is a 3-dimensional process, a more accurate 3-dimensional geometry of the system will also be desirable, but we expect our comparison of the different strategies to represent myosin ensembles in a simulation to remain relevant.

AUTHOR CONTRIBUTIONS

D.B.C., A.S.M, and F.N designed the research. D.B.C. carried out most of the simulations and data analysis. M.G. performed some simulations and assisted with data analysis. D.B.C. and A.S.M. wrote the manuscript with support from F.N.

ACKNOWLEDGEMENTS

The authors thank the members of the Maddox labs, especially Michael Werner, Jenna Perry and Tanner Fadero for critical reading of this manuscript. This work was supported by the NIH/NIGMS R01-102390 and NSF 1616661. Simulation work was run on the UNC Chapel Hill Research Computing Longleaf cluster.

SUPPORTING CITATIONS

References (42–44) appear in the Supporting Material.

REFERENCES

1. Green, A.R., E. Paluch, and K. Oegema. 2012. Cytokinesis in Animal Cells. Annu. Rev. Cell Dev. Biol. 28: 29–58.

2. Laplante, C., F. Huang, I.R. Tebbs, J. Bewersdorf, and T.D. Pollard. 2016. Molecular organization of cytokinesis nodes and contractile rings by super-resolution fluorescence microscopy of live fission yeast. Proc. Natl. Acad. Sci. 113: E5876–E5885.

3. Ding, W.Y., H.T. Ong, Y. Hara, J. Wongsantichon, Y. Toyama, R.C. Robinson, F. Nédélec, and R. Zaidel-Bar. 2017. Plastin increases cortical connectivity to facilitate robust polarization and timely cytokinesis. J. Cell Biol. 216: 1371–1386.

4. Wu, J-Q., Pollard, T.D. 2005. Counting Cytokinesis Proteins Globally and Locally in Fission Yeast. Science (80-.). 310: 310–314.

5. Courtemanche, N., T.D. Pollard, Q. Chen, N. Haven, and N. Haven. 2017. Avoiding artifacts when counting polymerized actin in live cells with Lifeact-fluorescent fusion proteins. 18: 676–683.

6. Wang, F., M. Kovacs, A. Hu, J. Limouze, E. V. Harvey, and J.R. Sellers. 2003. Kinetic Mechanism of Non-muscle Myosin IIB. J. Biol. Chem. 278: 27439–27448.

7. Kovács, M., F. Wang, A. Hu, Y. Zhang, and J.R. Sellers. 2003. Functional divergence of human cytoplasmic myosin II. Kinetic characterization of the non-muscle IIA isoform. J. Biol. Chem. 278: 38132–38140.

8. Billington, N., A. Wang, J. Mao, R.S. Adelstein, and J.R. Sellers. 2013. Characterization of three full-length human nonmuscle myosin II paralogs. J. Biol. Chem. 288: 33398–33410.

9. Laplante, C., J. Berro, A. Hernandez-leyva, R. Lee, T.D. Pollard, C. Laplante, J. Berro, E. Karatekin, A. Hernandez-leyva, and R. Lee. 2015. Three Myosins Contribute Uniquely to the Assembly and Constriction of the Fission Yeast Cytokinetic Article Three Myosins Contribute Uniquely to the Assembly and Constriction of the Fission Yeast Cytokinetic Contractile Ring. Curr. Biol. 25: 1955–1965.

10. Stachowiak, M.R., C. Laplante, H.F. Chin, B. Guirao, E. Karatekin, T.D. Pollard, and B. O'Shaughnessy. 2014. Mechanism of Cytokinetic Contractile Ring Constriction in Fission Yeast. Dev. Cell. 29: 547–561.

11. Vicente-manzanares, M., X. Ma, R.S. Adelstein, and A.R. Horwitz. 2009. Non-muscle myosin II takes centre stage in cell adhesion and migration. Nat Rev Mol Cell Biol. 10: 778–790.

12. Melli, L., N. Billington, S.A. Sun, J.E. Bird, A. Nagy, T.B. Friedman, Y. Takagi, and J.R. Sellers. 2018. Bipolar filaments of human nonmuscle myosin 2-A and 2-B have distinct motile and mechanical properties. Elife. 7: 1–25.

13. Murrell, M.P., and M.L. Gardel. 2012. F-actin buckling coordinates contractility

and severing in a biomimetic actomyosin cortex. Proc. Natl. Acad. Sci. .

14. Lenz, M., T. Thoresen, M.L. Gardel, and A.R. Dinner. 2012. Contractile Units in Disordered Actomyosin Bundles Arise from F-Actin Buckling. Phys. Rev. Lett. 108: 238107.

15. Ennomani, H., G. Letort, C. Guerin, J.L. Martiel, W. Cao, F. Nedelec, E.M. De La Cruz, M. Thery, and L. Blanchoin. 2016. Architecture and Connectivity Govern Actin Network Contractility. Curr. Biol. 26: 616–626.

16. Belmonte, J.M., M. Leptin, and F. Nédélec. 2017. A theory that predicts behaviors of disordered cytoskeletal networks. Mol. Syst. Biol. 13: 941.

17. Mendes Pinto, I., B. Rubinstein, A. Kucharavy, J.R. Unruh, and R. Li. 2012. Actin Depolymerization Drives Actomyosin Ring Contraction during Budding Yeast Cytokinesis. Dev. Cell. 22: 1247–1260.

18. Oelz, D.B., B.Y. Rubinstein, and A. Mogilner. 2015. A Combination of Actin Treadmilling and Cross-Linking Drives Contraction of Random Actomyosin Arrays. Biophys. J. 109: 1818–1829.

19. Ma, X., M. Kovács, M. Anne, A. Wang, Y. Zhang, and J.R. Sellers. 2012. Nonmuscle myosin II exerts tension but does not translocate actin in vertebrate cytokinesis. Proc. Natl. Acad. Sci. 109: 4509–4514.

20. Osorio, D.S., F.Y. Chan, J. Saramago, J. Leite, A.M. Silva, A.F. Sobral, R. Gassmann, and A.X. Carvalho. 2018. Flow-independent accumulation of motor-competent non-muscle myosin II in the contractile ring is essential for cytokinesis. .

21. Vasquez, C.G., S.M. Heissler, N. Billington, J.R. Sellers, and A.C. Martin. 2016. Drosophila non-muscle myosin II motor activity determines the rate of tissue folding. Elife. 5: 1–20.

22. Descovich, C.P., D.B. Cortes, S. Ryan, J. Nash, L. ZHang, P.S. Maddox, F. Nedelec, and A.S. Maddox. 2018. Cross-linkers both drive and brake cytoskeletal remodeling and furrowing in cytokinesis. Mol. Biol. Cell. 29: 622–631.

23. Li, Y., J.R. Christensen, K.E. Homa, G.M. Hocky, A. Fok, J.A. Sees, G.A. Voth, and D.R. Kovar. 2016. The F-actin bundler α-actinin Ain1 is tailored for ring assembly and constriction during cytokinesis in fission yeast. Mol. Biol. Cell. 27: 1821–1833.

24. Nagy, A., Y. Takagi, N. Billington, S.A. Sun, D.K.T. Hong, E. Homsher, A. Wang, and J.R. Sellers. 2013. Kinetic characterization of nonmuscle myosin IIB at the single molecule level. J. Biol. Chem. 288: 709–722.

25. Stam, S., J. Alberts, M.L. Gardel, and E. Munro. 2015. Isoforms confer characteristic force generation and mechanosensation by myosin II filaments. Biophys. J. 108: 1997–2006.

26. Erdmann, T., P.J. Albert, and U.S. Schwarz. 2013. Stochastic dynamics of small

ensembles of non-processive molecular motors: The parallel cluster model. J. Chem. Phys. 139.

27. Bidone, T.C., H. Tang, and D. Vavylonis. 2014. Dynamic network morphology and tension buildup in a 3D model of cytokinetic ring assembly. Biophys. J. 107: 2618–2628.

28. Bidone, T.C., W. Jung, D. Maruri, C. Borau, R.D. Kamm, and T. Kim. 2017. Morphological Transformation and Force Generation of Active Cytoskeletal Networks. PLoS Comput. Biol. 13.

29. Nguyen, L.T., M.T. Swulius, S. Aich, M. Mishra, and G.J. Jensen. 2018. Coarse-grained simulations of actomyosin rings point to a nodeless model involving both unipolar and bipolar myosins. Mol. Biol. Cell. 29: 1318–1331.

30. Nicholas, M.P., F. Berger, L. Rao, S. Brenner, C. Cho, and A. Gennerich. 2015. Cytoplasmic dynein regulates its attachment to microtubules via nucleotide state-switched mechanosensing at multiple AAA domains. Proc. Natl. Acad. Sci. 112: 6371–6376.

31. Dong, C., and B. Chen. 2015. Catch-slip bonds can be dispensable for motor force regulation during skeletal muscle contraction. Phys. Rev. E - Stat. Nonlinear, Soft Matter Phys. 92: 1–8.

32. Guo, B., and W.H. Guilford. 2006. Mechanics of actomyosin bonds in different nucleotide states are tuned to muscle contraction. Proc. Natl. Acad. Sci. 103: 9844–9849.

33. Nishizaka, T., H. Miyata, H. Yoshikawa, S. Ishiwata, and K. Kinosita. 1995. Unbinding force of a single motor molecule of muscle measured using optical tweezers. Nature. 377: 251–254.

34. Yamada, A., A. Mamane, J. Lee-Tin-Wah, A. Di Cicco, C. Prévost, D. Lévy, J.F. Joanny, E. Coudrier, and P. Bassereau. 2014. Catch-bond behaviour facilitates membrane tubulation by non-processive myosin 1b. Nat. Commun. 5: 3624.

35. Nedelec, F., and D. Foethke. 2007. Collective Langevin dynamics of flexible cytoskeletal fibers. New J. Phys. 9.

36. Pollard, T.D. 1986. Rate Constants for the Reactions of ATP- and ADP-Actin with the Ends of Actin Filaments. J. Cell Biol. 103: 2747–2754.

37. Daniels, B.R., B.C. Masi, and D. Wirtz. 2006. Probing Single-Cell Micromechanics In Vivo : The Microrheology of C . elegans Developing Embryos. 90: 4712–4719.

38. Niederman, R., and T.D. Pollard. 1975. Human Platelet Myosin. J. Cell Biol. 67: 72–92.

39. Sinard, J.H., W.F. Stafford, and T.D. Pollard. 1989. The mechanism of assembly of Acanthamoeba myosin-II minifilaments: minifilaments assemble by three successive dimerization steps. J. Cell Biol. 109: 1537–1547.

40. Bidone, T.C., W. Jung, D. Maruri, C. Borau, R.D. Kamm, and T. Kim. 2017. Morphological Transformation and Force Generation of Active Cytoskeletal Networks. PLoS Comput. Biol. 13: 1–22.

41. Bourdages, K.G., B. Lacroix, J.F. Dorn, C.P. Descovich, and A.S. Maddox. 2014. Quantitative analysis of cytokinesis in situ during C. elegans postembryonic development. PLoS One. 9.

42. Isambert, H., P. Venier, A. Maggs, A. Fattoum, R. Kassab, D. Pantaloni, and M. Carlier. 1995. Flexibility of actin filaments derived from thermal fluctuations. Effect of bound nucleotide, phalloidin, and muscle regulatory proteins. J. Biol. Chem. 270: 11437–11444.

43. Umemoto, S., and J.R. Sellers. 1990. Characterization of in vitro motility assays using smooth muscle and cytoplasmic myosins. J. Biol. Chem. 265: 14864–14869.

44. Thoresen, T., M. Lenz, and M.L. Gardel. 2011. Reconstitution of Contractile Actomyosin Bundles. Biophys. J. 100: 2698–2705.

FIGURE LEGENDS

Figure 1. Methods of modeling motor ensembles. A) (Top) Slip bond unbinding dynamics represented by bond lifetime over external force load (F_{ext}). (Middle) Catch bond unbinding dynamics represented by bond lifetime over external force-load. (Bottom) Catch slip bond unbinding dynamics represented by bond lifetime over external force-load. B) Schematic representation of NMMII motor ensemble with all motors discretely represented as gray rectangles. B') Representation of the ensemble shown in B interacting with filaments (gray) in a network. B") Representation of a fully coarse-grained ensemble with only two filament-binding domains representing all motors (purple) interacting with filaments (gray) in a network.

Figure 2. Coarse-grained slip bond ensembles are processive and generate contractility. A) Kymograph of coarse-grained monopolar motor complexes (red) moving on immobilized filaments. B) Time lapse frames of a contractile ring (black) with bipolar motors as shown in A, showing constriction. C) Kymograph of discretized monopolar motor complexes (pink) moving on immobilized filaments. D) Time lapse frames of a contractile ring (black) with bipolar motors as shown in B, showing failure of constriction and ring fragmentation. E) Graph of radial ingression speed normalized over closure of the ring in B. F) Graph of radial ingression speed normalized over ring closure of the ring in D. Light red areas and fills in graphs represent standard deviation. Translocation data n= 120 motor ensembles; contractile ring curves n = 20 simulations.

Figure 3. Coarse-grained catch bond ensembles are processive and generate contractility. A) Kymograph of coarse-grained monopolar muscle myosin II motor complexes (green) moving on immobilized filaments. B) Time lapse frames of a contractile ring (black) with bipolar motors as shown in A, showing rapid constriction. C) Kymograph of coarse-grained monopolar NMMII motor complexes (green) moving on immobilized filaments. D) Time lapse frames of a contractile ring (black) with bipolar motors as shown in D, showing partial failure of constriction and ring collapse. E) Graph of radial ingression speed normalized over closure of the ring in B. F) Graph of radial ingression speed normalized over ring closure of the ring in D. Light green areas and fills in graphs represent standard deviation. Translocation data n= 120 motor ensembles; contractile ring curves n = 20 simulations.

Figure 4. The effects of increasing discretization on catch bond motor ensembles. A) Graph of average translocation speeds on immobilized filaments for NMMII monopolar ensembles with parallel clusters (PCs) of 1, 2, 4, 8 or 16 motors each. Total motors per monopolar ensemble was constant at 16. Each data point represents the average of 120 ensembles over the course of 400 simulated seconds. B) Graph of maximum radial constriction speed for contractile rings simulated with bipolar NMMII ensembles of the 5 different types as before. Bipolar complexes all had a total of 32 motors. Each data point represents the average of 20 different contractile ring simulations. C) Graph of maximum closure for contractile rings simulated with bipolar NMMII ensembles of the five different types as in B. Each data point represents the average of 20 different contractile ring simulations. D) Graph od average percent of time bound for each type of monopolar

ensemble when seeded on immobilized filaments as in A. Percentage was calculated using the total time of simulation. Each data point represents the average of 120 ensembles over 400 seconds. Bars on all graphs represent standard deviation.

Figure 5. Discretized and coarse-grained catch-slip bond ensembles are processive and generate contractility. A) Kymograph of discretized NMMII motor complexes (blue) moving on immobilized filaments over time (Y-axis). B) Time lapse frames of a contractile ring (black) with bipolar motors as shown in A, showing constriction. C) Kymograph of coarse-grained NMMII motor complexes (dark blue) moving on immobilized filaments. D) Time lapse frames of a contractile ring (black) with bipolar motors as shown in C, showing constriction. E) Graph of radial ingression speed normalized over closure of the ring in B. F) Graph of radial ingression speed normalized over ring closure of the ring in D. Light blue areas in graphs represent standard deviation. Translocation data n= 120 motor ensembles; contractile ring curves n = 20 simulations.

Figure 6. Tuning ring connectivity affects contractile dynamics. A) Graph of the maximum radial closure speed for contractile rings versus the total connectivity of these simulations. Connectivity differences are the direct result of how many motors each PC is comprised of as in Figure 4. B) Graph of the maximal radial closure speed for contractile rings versus the NMMII connectivity. For A and B, each data point is the average of 20 simulated contractile rings. C) Graph showing the predicted relationship between total connectivity of contractile rings versus the total number of septin-like agents included in the simulation. D) Graph showing the relationship between total connectivity and maximum radial closure speed when connectivity is modulated via septin-like agent titration. Best fit curve is quadratic. For C and D, each point is a single simulation n = 100.

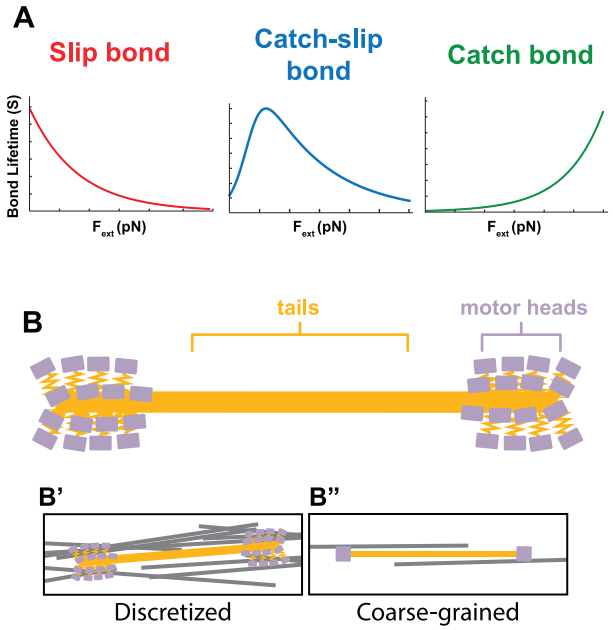
A
Slip bond
Catch-slip bond
Catch bond
Bond Lifetime (S)
F ext (pN)
F ext (pN)
F ext (pN)
B
tails
motor heads
B'
B''
Discretized
Coarse-grained

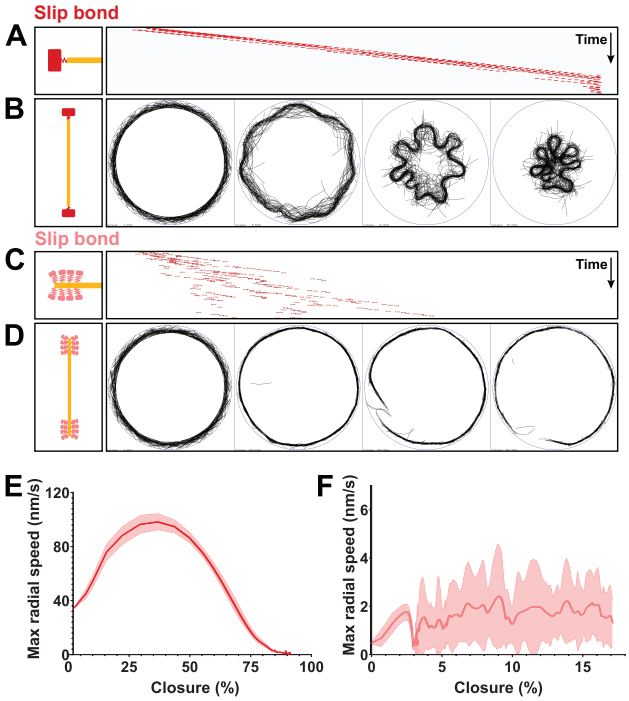
Slip bond
A
Time
B
Slip bond
C
Time
D
E
Max radial speed (nm/s)
120
80
40
0
0
25
50
75
100
Closure (%)
F
Max radial speed (nm/s)
6
4
2
0
0
5
10
15
Closure (%)

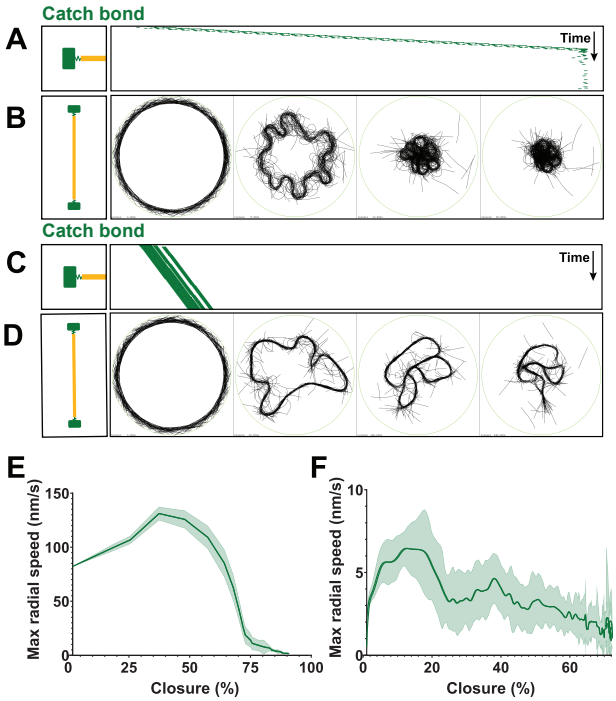
Catch bond
A
Time
B
Catch bond
C
Time
D
E
Max radial speed (nm/s)
150
100
50
0
0
25
50
75
100
Closure (%)
F
Max radial speed (nm/s)
10
5
0
0
20
40
60
Closure (%)

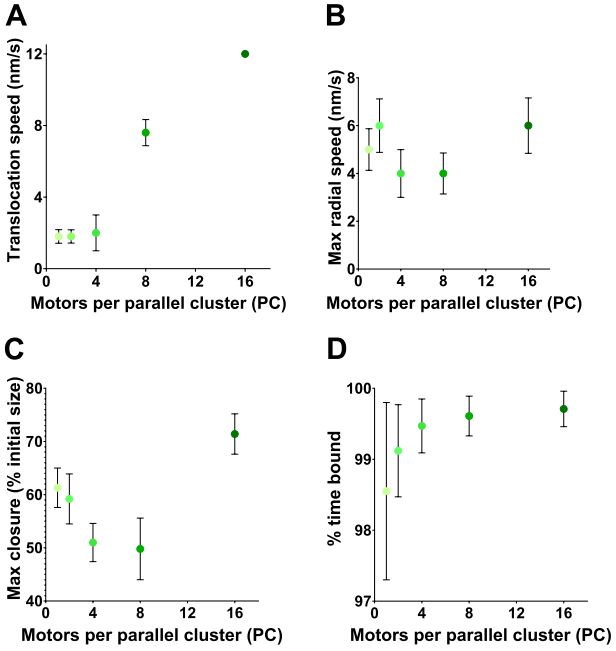
A
Translocation speed (nm/s)
0
4
8
12
0
4
8
12
16
Motors per parallel cluster (PC)
B
Max radial speed (nm/s)
0
2
4
6
8
0
4
8
12
16
Motors per parallel cluster (PC)
C
Max closure (% initial size)
40
50
60
70
80
0
4
8
12
16
Motors per parallel cluster (PC)
D
% time bound
97
98
99
100
0
4
8
12
16
Motors per parallel cluster (PC)

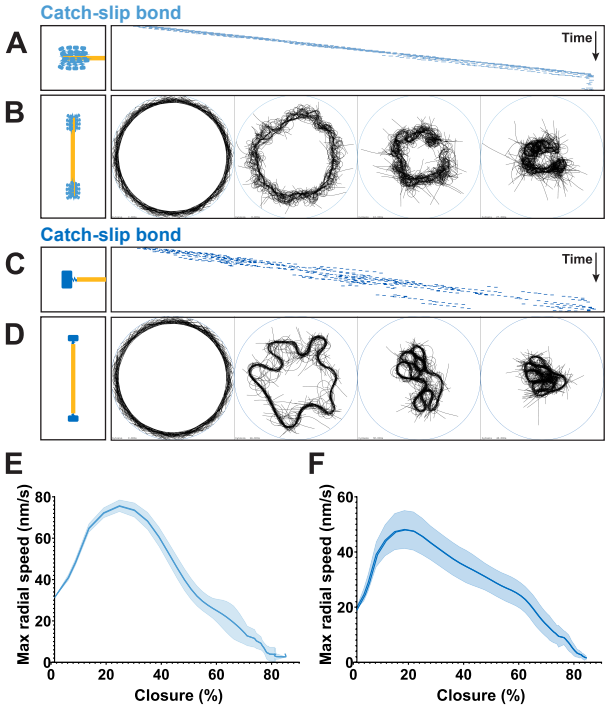
Catch-slip bond
A
Time
B
Catch-slip bond
C
Time
D
E
Max radial speed (nm/s)
Closure (%)
F
Max radial speed (nm/s)
Closure (%)

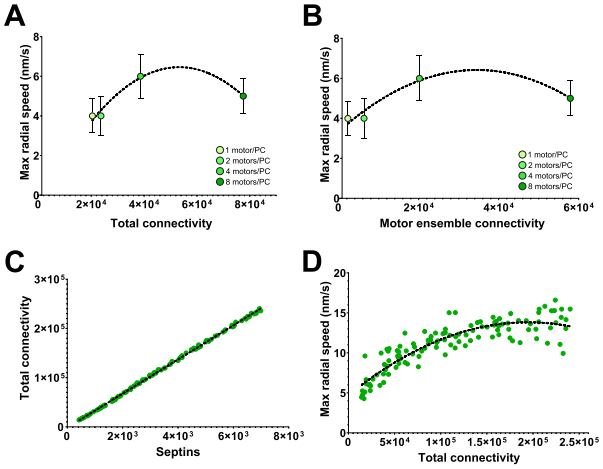
A
Max radial speed (nm/s)
Total connectivity
1 motor/PC
2 motors/PC
4 motors/PC
8 motors/PC
B
Max radial speed (nm/s)
Motor ensemble connectivity
C
Total connectivity
Septins
D
Max radial speed (nm/s)
Total connectivity